Search for entanglement in the decay dynamics and anisotropic emission of a pair of H($2p$) atoms produced by XUV photodissociation of H_2

A. Dochain,[1,*] B. Fabre,[2] C. Lauzin,[1] and X. Urbain[1,†]

[1] *Institute of Condensed Matter and Nanosciences, Université catholique de Louvain, B-1348 Louvain-la-Neuve, Belgium*

[2] *Université de Bordeaux-CNRS-CEA, CELIA, UMR5107, F33405 Talence, France*

The production of pairs of correlated Lyman-α photons upon XUV excitation of molecular hydrogen is studied using coincidence measurements to evaluate at which level the entanglement is transferred from atoms to photons. By referencing the timing of fluorescence photon detection to the synchrotron light pulse, we were able to determine branching ratio for the $2p+2p$ and $2p+3\ell$ (with $\ell = s, d$) channels separately. Time dependent analysis of the spectral signature recorded around 33.6 eV and close examination of the doubly excited states lying in the Franck-Condon window confirm prior assignments of the $2p+2p$ being the main dissociation channel of the Q_2 $^1\Pi_u$ (1) molecular state. The angular dependence of the two-photon detection probability measured with respect to the polarization axis is found to be in agreement with earlier measurements (Phys. Rev. A **99**, 063426 (2019)). A simple model, assuming a transition from Hund's case (a) to Hund's case (c), reproduces the measured angular distributions satisfactorily.

I. INTRODUCTION

Homonuclear diatomic molecules have long been contemplated as a natural source of entangled atom and photon pairs through dissociation and electronic excitation respectively. Molecules were thus considered suitable for a direct test of Bell's inequalities with actual spins as suggested by Bohm [1], instead of polarization states of light as performed by Clauser [2], Aspect [3] and Zeilinger [4]. As a result of molecular photodissociation, a pair of entangled atoms is generated. Interrogating such Einstein-Podolsky-Rosen (EPR) pairs involves either a spin analyser of the Stern-Gerlach type for H_2 [5, 6] or some multiphoton ionization scheme for Hg_2 or Cd_2 [7–9]. This approach was later extended to polyatomic systems where photodissociation leads to entanglement between internal degrees of freedom of the fragment molecule and momentum of the recoiling atom [10]. More recently, the possibility of launching entangled atom pairs by exciting a Bose-Einstein condensate on an atom chip has been demonstrated [11].

In this context, the characterization and potential control of entanglement/disentanglement has attracted numerous studies since the first measurement of the Lyman-α–Lyman-α coincidence spectrum coming from the dissociation of doubly excited molecular hydrogen [12]. These two Lyman-α photons mainly come from the deexcitation of a pair of H($2p$) atoms produced by photodissociation of H_2 [13]:

$$H_2 + h\nu_{XUV} \rightarrow H_2^{**}\left(Q_2\ ^1\Pi_u\right) \rightarrow H(2p) + H(2p). \quad (1)$$

Following the development of synchrotron facilities, new experimental and theoretical studies have been conducted with the aim of characterizing the two-photon entanglement [14–18]. In particular, in [14, 15], the authors claimed to observe the effect of entanglement via the shortening of the emission lifetime of the atomic H($2p$) states. This statement was also supported by the analysis of the angular correlation function (ACF) of the double Lyman-α emission. The entanglement of the two H($2p$) atoms, even separated by a large distance, was assumed to be transferred to the two emitted photons [19]. None of these previous experimental studies was able to measure the initial time t_0 corresponding to absorption of the XUV excitation photon.

In this paper, we aim at characterizing the entanglement of the two Lyman-α photons by performing a complete coincidence measurement of the two Lyman-α emission, with the addition of an initial reference time provided by a synchrotron clock. In Section II, the experimental coincidence setup is presented. We describe in Section III the decay dynamics of the two Lyman-α photon emission with the ability to determine the arrival time of the first and second photon, and compare the experimental distribution with several models (atomic spontaneous decay, superradiance and entangled photon emission). In Section IV, we explain how to isolate the coincident two-photon emission coming from the deexcitation of a pair of H($2p$) atoms produced by the dissociation of a single molecule from Lyman-α photons emitted from separate molecules or resulting from other photodissociation and deexcitation paths. This allows us to obtain the partial cross section for the H($2p$) + H($2p$) and H($2p$) + H($3d$) channels as a function of the synchrotron XUV photon energy. Finally, in Section V, we analyze the angular dependence of the two-photon emission with respect to the polarization axis of the XUV exciting beam. In this section we also develop a model for the ACF taking into account the experimental constraints of the measurement. This model does not rely on

* Present address: Department of Physics, Stockholm University, SE-10691 Stockholm, Sweden.

† xavier.urbain@uclouvain.be

an entangled photon emission and matches the observations while preserving the *ungerade* character of the final H($1s$) atom pair. All necessary developments regarding decay probabilities and molecular symmetries are given in Appendices A and B.

II. EXPERIMENTAL SETUP AND METHOD

The experimental setup is presented in Fig. 1. The DESIRS beamline of the SOLEIL synchrotron facility was used as a pulsed source of XUV photons with tunable polarization and wavelength. This source, when operating in single bunch mode, is characterized by a repetition rate of 846 kHz and an average number of 2.5×10^{10} photons per second at 33 eV for a bandwidth of 0.1%. Each pulse has a temporal full width at half maximum (FWHM) of 60 to 70 ps [20].

A trigger associated with the arrival time t_0 of the pulse was provided by the SOLEIL synchrotron clock through a fast Transistor-Transistor-Logic (TTL) signal. The jitter of the TTL with respect to the synchrotron master clock is of 1 to 2 ps. The relative intensity of the light pulses was monitored by a Faraday cup (FC) in Daly geometry [21], through the measurement of the electron current produced from the illumination of an electrically biased stainless steel plate by the XUV radiation. The readout was calibrated against the beamline photon flux monitor. This arrangement also allowed us to check the alignment of the XUV beam with respect to the axis of the interaction chamber.

The synchrotron beam was injected through a pair of circular apertures into an interaction cell at ambient temperature filled with molecular hydrogen at pressures ranging from 2×10^{-4} to 10^{-2} mbar. On either side of the cell, a CsI-coated multichannel plate assembly (MCP1 and MCP2, active diameter 29 mm), located behind a 1 mm-thick MgF_2 window at a distance of 21 mm from the synchrotron beam axis, was used to detect in coincidence the two Lyman-α photons emitted by H($2p$) pairs at time t_1 and t_2. The synchrotron clock trigger t_0 (S), and the photon arrival times t_1 (MCP1) and t_2 (MCP2) were recorded by a multichannel time-to-digital converter (TDC) with 120 ps bin width. The start signal (or common stop signal) was generated by S AND MCP1 AND MCP2 or by S AND (MCP1 OR MCP2) as illustrated in Fig. 1. The use of logical operators OR and AND ensures the correct discrimination of coincident events from single photon detection. All timing signals were amplified and treated by a constant fraction discriminator (CFD) before being recorded.

The completeness of the present study, where all times are measured, constitutes a major experimental improvement with respect to the study of Tanabe *et al.* [15]. The previous measurements [12, 22] exhibit a clear maximum located at 33.6 eV. Accordingly, this incident photon energy was chosen to perform the measurements presented hereafter.

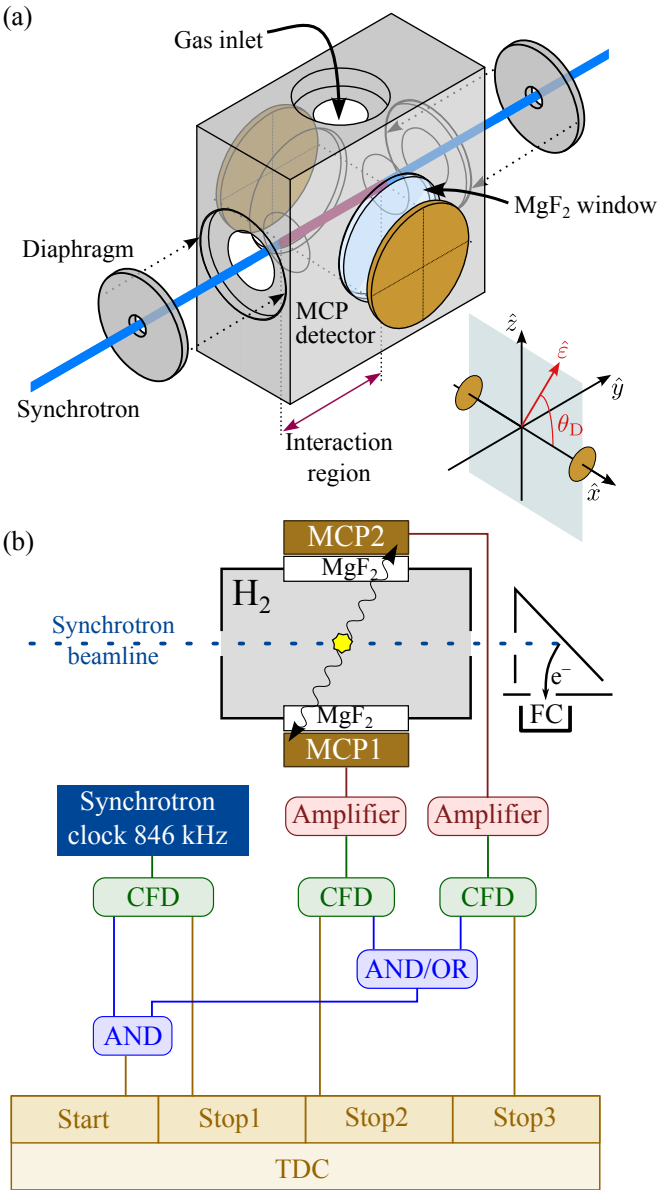

Figure 1. (a) Experimental setup. The interaction region between the synchrotron radiation and the H_2 gas is highlighted in purple. In this configuration, the angle between the synchrotron polarization direction $\hat{\varepsilon}$ and the inter-detector axis (aligned along $\hat{x}$) is given by θ_D. (b) Schematic representation of the experimental setup. CFD stands for Constant Fraction Discriminator, TDC for Time-to-Digital Converter, MCP for Multichannel Plate and FC for Faraday Cup.

As illustrated in Fig. 1, this configuration, where three time stamps (t_0, t_1 and t_2) are recorded per coincidence gives us several ways of visualizing the H($2p$) fluorescence histograms, either by plotting the decay measured on each detector referenced to the clock, or by plotting the arrival time of the first and second photon with respect to the clock. An additional visualization was adopted by Tanabe and coworkers [15] in the absence of a reference clock, *i.e.* the time difference between detections,

$t_1 - t_2$. The detection signals were measured at two H_2 interaction cell pressures: a relatively high pressure (0.3 Pa) where no entanglement effect was expected, and a lower pressure (0.02 Pa) where the entanglement effect had been reported [14, 15].

In previous studies [13–15], the authors have measured the time difference between their two detectors and claimed to observe an effect of the gas pressure on the H($2p$) lifetime which they attributed to the loss of entanglement at high pressure. They originally concluded that the apparent lifetime of each of the entangled H($2p$) atom (low pressure case) was half that of an isolated H($2p$) atom. This observation was the original motivation of the present study. That assumption was however challenged by the same group, attributing this pressure effect to false coincidences due to cosmic muons. As mentioned in [23], the measurement of the absolute emission time of the first (t_f) and second (t_s) Lyman-α photon should provide sufficient information to draw a clear conclusion.

The decay times Δt_1 and Δt_2 measured respectively on detector 1 and 2 with respect to the XUV pulse, and defined as $\Delta t_1 = t_1 - t_0$ and $\Delta t_2 = t_2 - t_0$, are presented in Fig. 2 at low and high pressure (resp. 0.02 Pa in (a) and 0.3 Pa in (b)). For a given H_2 pressure, the two decay curves are superimposed, which confirms that the electronic response of the two detectors is identical. Additionally, the perfect mirroring of curves (a) and (b) shows that there is no pressure effect on the decay times, hence no factor of 2 reduction of the apparent $2p$ lifetime contrary to what was first reported [14, 15] and later invalidated [17].

In Fig. 3 are presented the arrival time of the first photon $t_f = \min(t_1, t_2) - t_0$ and that of the second one $t_s = \max(t_1, t_2) - t_0$. The arrival time of the first photon t_f presents a faster decay than the arrival time of the second photon t_s, as we discuss below.

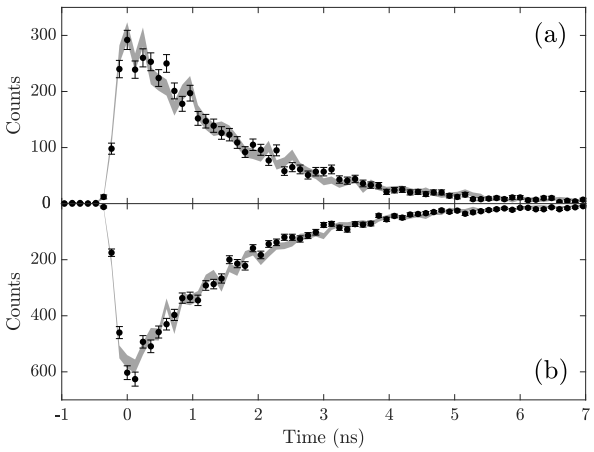

Figure 2. Decay time histograms of Δt_1 (shaded area: experiment with 1σ uncertainty interval) and Δt_2 (black dots with error bars: experiment with 1σ uncertainty interval) at a H_2 pressure of (a) 0.02 Pa and (b) 0.3 Pa. Recording time was adapted to reach the same statistics.

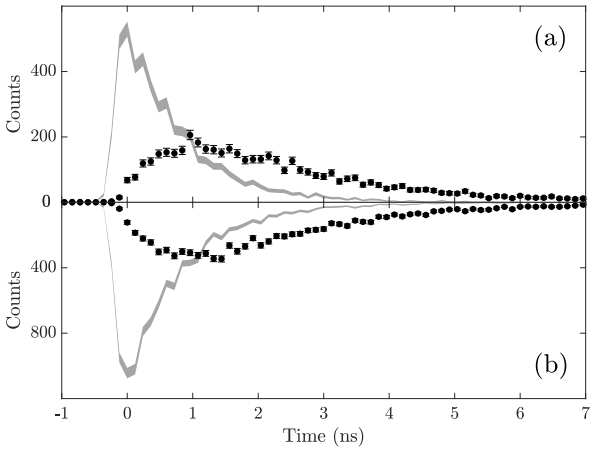

Figure 3. Decay time histograms of t_f (shaded area: experiment with 1σ uncertainty interval) and t_s (black dots with error bars: experiment with 1σ uncertainty interval), the respective time of arrival of the first and second photon, at a H_2 pressure of (a) 0.02 Pa and (b) 0.3 Pa.

III. DECAY DYNAMICS

The H($2p$) atom pair produced by reaction (1) will return to the ground state following the radiative cascade depicted in Fig. 4. Several models that could explain this decay process were proposed, as detailed below and will be compared to the experimental distribution in order to validate which model describes best the decay dynamics.

First, one could consider that the two atoms are independent. In such case, the emission dynamics is limited to spontaneous decay (SP) where the intermediate ($1s$,$2p$) states of the radiative cascade are not mixed nor entangled, leading to two distinct decay paths going through H($1s$)+H($2p$) or H($2p$)+H($1s$), respectively (see Fig. 4). The emission rates for the first and second photon obtained with such assumptions are:

$$p_f^{\mathrm{SP},2p}(t) = 2\Gamma e^{-2\Gamma t} \tag{2}$$

$$p_s^{\mathrm{SP},2p}(t) = 2\Gamma e^{-\Gamma t}\left(1 - e^{-\Gamma t}\right) \tag{3}$$

where Γ is the emission rate for the H(1s) $\leftarrow$ H(2p) transition (see Appendix A). In this framework, the emission rate of the first photon is twice the rate of an isolated H($2p$) atom without invoking any entanglement.

Superradiance theory (SUP), where the increase of the emission rate with respect to the case of isolated atoms is due to collective photon emission, could also be considered to explain this faster decay. The superradiance effect is directly related to the phase locking of the atomic dipoles through the medium, which is possible if the distance between the excited atoms is small compared to the emission wavelength [24]. In the absence of initial

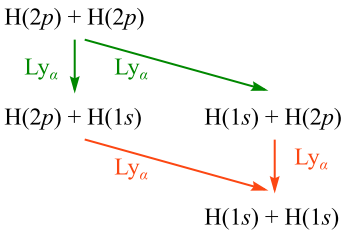

Figure 4. Radiative cascade following photodissociation of H_2 into a pair of H($2p$) atoms. Green arrows indicate the first Lyman-α (Ly$_\alpha$) photon, red arrows the second Lyman-α photon.

dipole-dipole correlation, the system decays to a superposition of H($1s$) + H($2p$) and H($2p$) + H($1s$) by emitting a first Lyman-α photon with a decay constant equal to 2Γ, meaning that the first photon obeys Eq. (2). This entangled state decays to the ground state of the two atoms with the same average rate 2Γ as for independent spontaneous emission. However, while the initial state contains two excited atoms, the second contains only one. According to Gross and Haroche [24], the emission rates $p_f^{\rm SUP}$ and $p_s^{\rm SUP}$ of the first and second photon over time t are obtained by time differentiation of initial and final populations (see Eqs. 2.26 and 2.28 from [24]):

$$p_f^{\rm SUP}(t) = 2\Gamma e^{-2\Gamma t} \tag{4}$$

$$p_s^{\rm SUP}(t) = 4\Gamma^2 t e^{-2\Gamma t}. \tag{5}$$

Whereas the equations describing the first photon emission are the same for both theories, the emission rate of the second photon differs, the superradiant emission presenting a faster decay than the spontaneous one.

To compare with experimental measurements, the decay curves of these two models have been convoluted with a Gaussian of 120 ps FWHM to take into account the time resolution of the TDC ($\sim$ 60 ps) and the synchrotron pulse duration ($\sim$ 60 − 70 ps). The experimental data have been normalized to a total of 2 emitted photons.

In order to perform the background subtraction, the sorted and integrated distribution of background (BG) events, as well as the coincidence between background counts and Lyman-α photons, were evaluated (see Appendix A 3). The background level is found to be between 1 and 3%.

The agreement between experiment and the spontaneous emission model, when using the decay constant given by the NIST [25] for the H($2p$) deexcitation, $\Gamma = 6.2649 \times 10^8$ s^{-1}, in Eqs. 2 and 3, is unambiguously better than the agreement with the superradiance prediction (see Fig. 5). This should not come as a surprise, in view of the approximate distance traveled by the departing atoms over a time $\tau = 1.6$ ns at a relative velocity $v \simeq 5.8 \times 10^6$ cm s^{-1} [26], $d \simeq v\tau = 93$ μm.

The agreement between the spontaneous decay theory and the experimental data can be further improved by

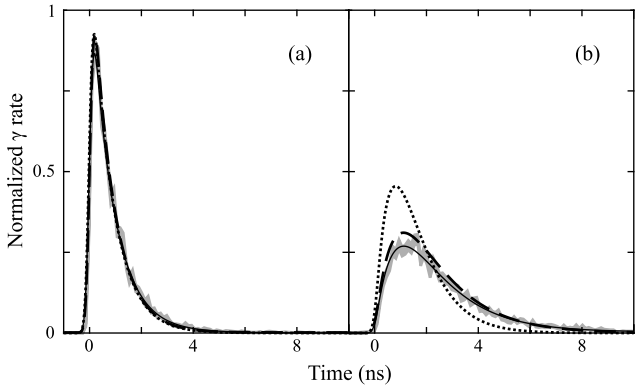

Figure 5. Comparison between theory and experiment for the normalized emission rate of the first (a) and second (b) photon at 0.02 Pa, $h\nu_{\rm XUV} = 33.6$ eV, $\theta_{\rm D} = 90°$ (see Fig. 1). Shaded area: experiment with 1σ uncertainty interval; Dotted curves: superradiance; Dashed curves: $(2p, 2p)$ spontaneous emission; Full curves: combined $(2p, 2p)$ and $(2p, 3d)$ spontaneous emission. Theoretical curves are convoluted by a Gaussian of 120 ps FHWM (see text).

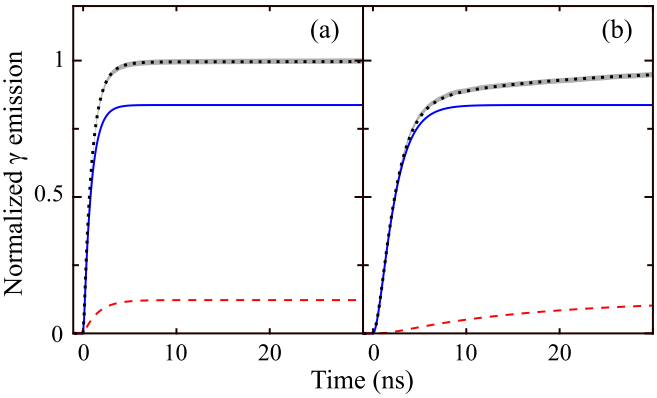

Figure 6. Comparison between theory and experiment for the normalized photon emission probability of the first (a) and second (b) photon at 0.02 Pa, $h\nu_{\rm XUV} = 33.6$ eV, $\theta_{\rm D} = 90°$ (see Fig. 1). Shaded area: experiment with 1σ uncertainty interval; Solid blue curves: $2p - 2p$ spontaneous emission component; Red dashed curves: $2p - 3\ell$ spontaneous emission component; Black dotted curves: total emission signal.

taking into account additional deexcitation channels following the dissociation of H_2^{**} (see Section IV):

$$H_2 + h\nu_{\rm XUV} \rightarrow H_2^{**} \rightarrow H(2p) + H(3s, 3d). \tag{6}$$

The $2p \leftarrow 3s, 3d$ transition leads to the emission of a Balmer-α photon (noted H_α). This photon, due to its wavelength, cannot be detected with our experimental arrangement, and its emission will precede that of the second Lyman-α (Ly$_\alpha$) photon. The intricate radiative cascade that ensues is depicted in Fig. 7. This cascade has a non-negligible influence on the two-photon decay rate. Indeed, as shown in Fig. 6, this extra deexcitation step will add a tail to the decay dynamics at late times.

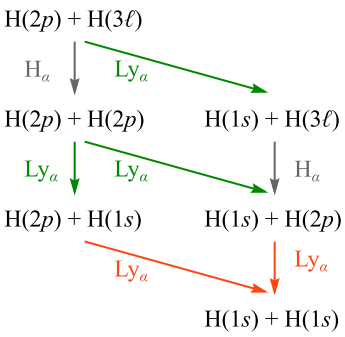

Figure 7. Radiative cascade including $(2p, 3\ell)$ channels, with $\ell = s, d$. Green arrows indicate the first Lyman-α (Ly_α) photon, red arrows the second Lyman-α photon and gray arrows the Balmer-α (H_α) photons. Only the Lyman-α photons are detected in the present experiment.

Dissociation of H_2^{**} via different Q_2 states leads to a mixed initial state represented as a combination of the $(2p, 2p)$ and $(2p, 3\ell)$ states, where $\ell = s, d$. The identification of the Q_2 states involved will be discussed at length in Section IV. The total spontaneous emission for this $(2p, 3\ell)$ state is given by (Appendix A 3):

$$p_f^{\mathrm{SP},3\ell} = \frac{\Gamma_{2p} e^{-\Gamma_{2p}t}}{\Gamma_{2p} - \Gamma_{3\ell}} \left[\left(\Gamma_{2p} + \Gamma_{3\ell}\right) e^{-\Gamma_{3\ell}t} - 2\Gamma_{3\ell} e^{-\Gamma_{2p}t} \right] \tag{7}$$

$$p_s^{\mathrm{SP},3\ell} = \frac{\Gamma_{2p}}{\Gamma_{2p} - \Gamma_{3\ell}} \Big[\left(\Gamma_{2p} - 2\Gamma_{3\ell}\right) e^{-\Gamma_{2p}t} + 2\Gamma_{3\ell} e^{-2\Gamma_{2p}t} - \left(\Gamma_{2p} + \Gamma_{3\ell}\right) e^{-(\Gamma_{2p}+\Gamma_{3\ell})t} + \Gamma_{3\ell} e^{-\Gamma_{3\ell}t} \Big]. \tag{8}$$

A linear combination of the decay probabilities $p_f^{\mathrm{SP},2p}$, $p_s^{\mathrm{SP},2p}$, $p_f^{\mathrm{SP},3\ell}$, and $p_s^{\mathrm{SP},3\ell}$ (Eqs. (2)-(3) and (7)-(8)) given the form:

$$R_f(t) = a_{2p}\, p_f^{\mathrm{SP},2p} + a_{3\ell}\, p_f^{\mathrm{SP},3\ell} \tag{9}$$

$$R_s(t) = a_{2p}\, p_s^{\mathrm{SP},2p} + a_{3\ell}\, p_s^{\mathrm{SP},3\ell} \tag{10}$$

is fitted to the experimental emission rate measurements while keeping as fixed parameters $\Gamma_{3d} = \Gamma_{2p\leftarrow 3d} = 0.064$ ns^{-1}, $\Gamma_{3s} = \Gamma_{2p\leftarrow 3s} = 0.0063$ ns^{-1} and $\Gamma_{2p} = \Gamma_{1s\leftarrow 2p} = 0.625$ ns^{-1} as tabulated by NIST [25]. As the coincidence range and the analytical shape of $p_s^{\mathrm{SP},3\ell}$ are known, the amount of undetected events is included in the yield (see Appendix A 2). This is best achieved by working with the integrated photon yield and analytical decay probabilities (see Appendix A 3). The χ^2 fit of the data given in Figs. 5 and 6 gives a branching ratio of $80.8 \pm 1.3\%$ for $(2p, 2p)$, $12.6 \pm 1.5\%$ for $(2p, 3d)$ and $6.6 \pm 2.2\%$ for $(2p, 3s)$. This ratio is compatible with the $\mathrm{Ly}_\alpha/\mathrm{H}_\alpha$ cross section ratio measured by Glass-Maujean [27] for the photodissociation of H_2. Considering the small proportion of $(2p, 3s)$ and the two orders of magnitude longer lifetime of $3s$ compared to $2p$, it is difficult to separate its decay dynamics from the $2p$-background coincidences for coincidence windows shorter than 60 ns (see Appendix A 5), leading to an additional uncertainty in the fit. Since the $(2p, 3s)$ contribution could not be extracted from some of our measurements, only $(2p, 3d)$ is considered in the remainder of the text.

Although nearly no change can be seen in the instantaneous decay rate, those higher lying levels have a significant effect on the cumulative distribution of emitted photons over time. The improvement of the model through the inclusion of this dynamics is clearly visible in Fig. 6.

Sancho and Plaja [23] have proposed an alternative way to describe the emission of two photons coming from the deexcitation of entangled atom pairs. Following their development, the decay rates for the first and second photon may be written as:

$$p_f^{\mathrm{S\&P}} = \Gamma_f e^{-\Gamma_f t} \tag{11}$$

$$p_s^{\mathrm{S\&P}} = \frac{\Gamma_f \Gamma_s}{\Gamma_s - \Gamma_f} \left(e^{-\Gamma_f t} - e^{-\Gamma_s t} \right) \tag{12}$$

This description is compatible with the spontaneous emission model when the decay constants for the first and second photon are respectively taken equal to $\Gamma_f = 2\Gamma$ and $\Gamma_s = \Gamma$. However, they do not necessarily assume those values. The decay rate and photon emission described by Sancho and Plaja are not plotted in Fig. 5 as the fit gives $\Gamma_f = (1.94 \pm 0.08)\Gamma$ and $\Gamma_s = (0.99 \pm 0.10)\Gamma$, meaning they are perfectly superimposed to the spontaneous emission ones.

Although they provide information on the deexcitation path, absolute emission time measurements do not allow us to discriminate the independent spontaneous emission model from the entangled model of Sancho and Plaja [23]. This unique observable is thus not sufficient to reach a definite conclusion about the role of entanglement in the emission dynamics of the Lyman-α photon pair.

IV. PARTIAL CROSS SECTIONS

The spectral dependence of the coincidence signal may be used to further confirm the leading $(2p, 2p)$ and $(2p, 3d)$ contributors to the two-photon emission. In order to extract partial cross sections, the coincidence rate was measured as a function of gas pressure and synchrotron XUV photon energy, as presented in Figs. 8 and 9, respectively. The signal-to-noise ratio was excellent ($60:1$ to $1200:1$), as we measured less than one coincidence per minute with the XUV beam off and always above 1 Hz with the XUV beam on. The measurement of the partial cross sections versus photon energy was performed with linear polarization along the z-axis (vertical polarization, perpendicular to the inter-detector axis).

A linear dependency of the signal with the pressure ensures that the two coincident photons come from the same molecule, and is hence proportional to the cross section, while a quadratic pressure dependency indicates

that the two detected Lyman-α photons were emitted from different molecules.

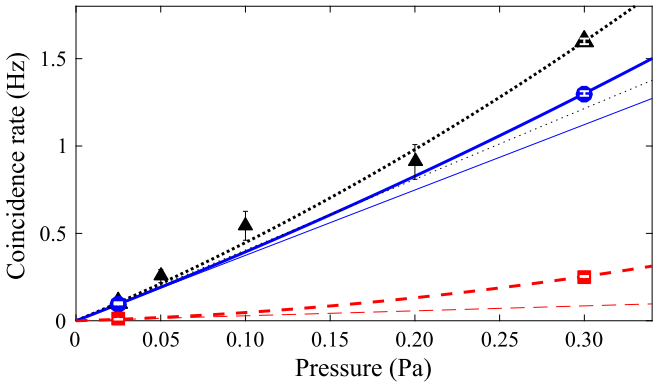

Figure 8. Pressure dependence of the total (black triangles), partial $(2p, 2p)$ (blue dots) and $(2p, 3d)$ (red squares) coincidence rates measured with vertically polarized (along the z-axis) incident photons at 33.6 eV. The partial coincidence rates are obtained using the fit shown in Fig. 6. Quadratic fit (thick lines) and linear fit (thin lines) are shown for the total (dotted lines), the $(2p, 2p)$ (blue full lines) and the $(2p, 3d)$ (red dashed lines) components.

The $3d/2p$ ratio was extracted from the fit of the decay dynamics shown in Fig. 9, and the partial cross sections versus photon energy are shown in Fig. 11. As the decay dynamics is the same whether the Lyman-α photons originate from one or several H_2 molecules, the fitting procedure remains valid for both the true coincidences (pair of photons emitted by a single molecule) and the false coincidences (pair of photons emitted by different molecules). This allows us to determine that the signal at 0.02 Pa mostly consists of true coincidences for both channels, while the delayed signal corresponding to $3d$ cascade comes mostly from false coincidences at higher pressure.

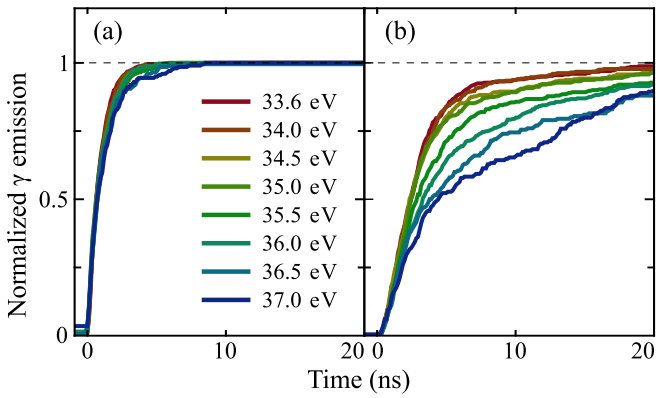

Figure 9. Decay dynamics at various photon energies (33.6 eV to 37 eV). First photon emission (a), second photon emission (b). The increasing contribution of the $(2p, 3\ell)$ is clearly visible.

The false coincidences are removed from the apparent cross section using a global quadratic fit of the coincidence rate as a function of pressure, as shown in Fig. 8. The total number $N_{2pn\ell}$ of coincidences measured over a time T associated with the state $(2p, n\ell)$ is assumed to be given by:

$$\frac{N_{2pn\ell}}{T} = \alpha_{2pn\ell}(E_\gamma, \hat{\varepsilon}) P I_\gamma + [\beta_{2p}(E_\gamma, \hat{\varepsilon}) P I_\gamma]\,[\beta_{n\ell}(E_\gamma, \hat{\varepsilon}) P I_\gamma] \qquad (13)$$

where P is the cell pressure, I_γ is the synchrotron photon flux, $\hat{\varepsilon}$ is the polarization direction of the incident photon, $\alpha_{2pn\ell}(E_\gamma, \hat{\varepsilon})$ is proportional to the doubly differential photodissociation cross section toward the corresponding doubly excited states (Fig. 11), and $\beta_{n\ell}(E_\gamma, \hat{\varepsilon})$ is proportional to the partial photodissociation cross section toward both singly and doubly excited states for which only one photon is detected (Fig. 10). Among the latter processes embodied by $\beta_{n\ell}(E_\gamma, \hat{\varepsilon})$, let us mention the photodissociation via Q_1 states forming $H(1s)+H(n\ell)$ and their subsequent radiative deexcitation.

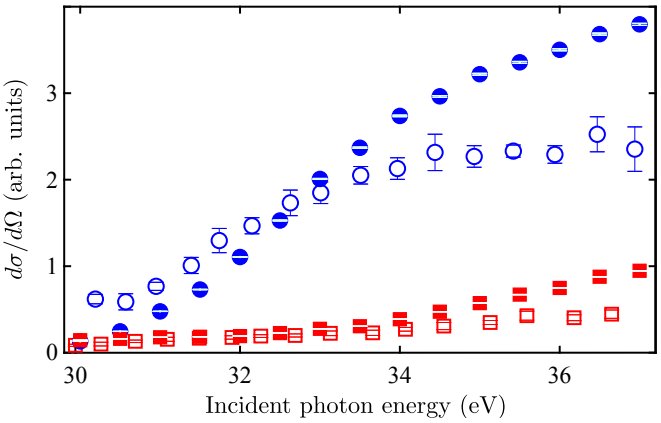

Figure 10. Singly differential cross section for the emission of Lyman-α (blue circles) or Balmer-α (red squares) photons as a function of the XUV photon energy. Filled circles and squares: this work ($\theta_D = 90°$ and Balmer-α values are deduced from delayed $2p$ emission); Open circles and squares: Glass-Maujean [27].

The latter is estimated using non-coincident measurements for which the $2p/3d/BG$ count rate was extracted from the decay dynamics (similarly as in Section III). The magnitude of the $\beta_{n\ell}(E_\gamma, \hat{\varepsilon})$ parameters was obtained at $E_\gamma = 33.6$ eV from the quadratic fit of the coincidence rate *vs* pressure while their energy dependence is identified to the evolution of the single photon signal as shown in Fig. 10. By subtracting this quadratic term from the total signal for all photon wavelengths, one obtains the energy dependence of $\alpha_{2pn\ell}(E_\gamma, \hat{\varepsilon})$ hence of the partial cross section of interest.

These partial cross sections are shown in Fig. 11 as a function of the XUV photon energy. They fall in good agreement with previous measurements by Odagiri *et al.* [22] and Hosaka *et al.* [28], the latter being of superior statistical significance. The error associated with present

partial cross sections is the combination of statistical uncertainty, χ^2 fit error of Eqs. (9) and (10) – which include the timing precision of the decay process –, 5% precision on the pressure reading and $\sim 1\%$ precision in the determination of the synchrotron flux. All those errors are propagated using Eq. (13) and its single photon equivalent, and finally combined using the square root of the sum of the square of each identified significant source of uncertainty.

The larger values obtained by Odagiri *et al.* [22] and Hosaka *et al.* [28] when the incident photon energy is higher than 35 eV might come from a contamination of the H(2p) + H(2p) by the H(2p) + H(3d) signal. This effect is small with Odagiri *et al.* who used a 50 ns coincident time window (only 5% of the H(2p) + H(3d) signal is lost), albeit with an alternate detector orientation (detectors located along the polarization axis instead of perpendicular to it). Hosaka *et al.* removed the H(2p) + H(3d) signal by fitting the decay dynamics with the H(2p)+H(2p) curve plus a constant background signal. As the H(2p) + H(3d) signal corresponds to neither of these curves for the 16 ns coincident window they used, (40% of H(2p) + H(3d) signal is lost in such case – see Appendix A 5, Fig. 14), it is difficult to assess which proportion of the signal comes from the H(2p) + H(3d) decay dynamics.

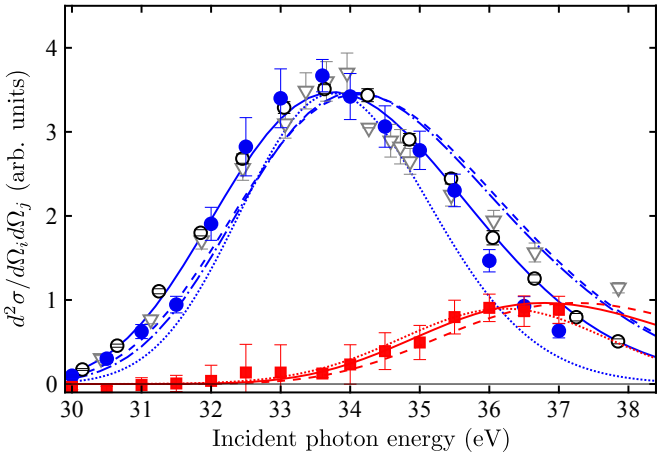

Figure 11. Doubly differential cross section for the emission of two Lyman−α photons as a function of incident photon energy. Polarization is set perpendicular to the detection axis ($\theta_D = 90°$). $(2p, 2p)$ partial cross section: filled blue circles – present experiment; open gray triangles – Odagiri *et al.* [22]; open black circles – Hosaka *et al.* [28]. $(2p, 3\ell)$ partial cross section: filled red squares – present experiment. Q_2 $^1\Pi_u(1)$: full blue line – linear dipole matrix element; long dashed blue line – constant dipole matrix element; dot-dashed blue line – matrix element from Borges & Bielschowsky [29]; short dashed blue line – model calculation from Glass-Maujean & Schmoranzer [30]. Q_2 $^1\Sigma_u^+(2)$: full red line – linear dipole matrix element; long dashed red line – constant dipole matrix element; dot-dashed red line – matrix element from Borges & Bielschowsky [29]; short dashed red line – model calculation from Glass-Maujean & Schmoranzer [30].

Numerous theoretical attempts to reproduce the actual excitation function of Lyman-α and Balmer-α emission have been performed, at various levels of theory [27–37]. All calculations rely on the accuracy of the potential energy curves of the autoionizing states lying in the Franck-Condon window [38] and located far above the ionization threshold of H_2 [39], and the knowledge of their dynamical correlation to the atomic asymptotes leading to line emission.

Such states have an excited ionic core and form Rydberg series converging to the excited molecular orbitals of H_2^+: Q_1 with $2p\sigma_u$, Q_2 with $2p\pi_u$, Q_3 with $2s\sigma_g$ [38, 40, 41]. As a result of the double degeneracy of the atomic asymptotes, two molecular orbitals correlate with every atomic asymptote, *e.g.* $1s\sigma_g$ and $2p\sigma_u$ with H(1s)+H$^+$, $2s\sigma_g$ and $3p\sigma_u$ with H(2s)+H$^+$, $3d\sigma_g$ and $4f\sigma_u$ with H(2p_0)+H$^+$, $2p\pi_u$ and $3d\pi_g$ to H(2$p_{\pm1}$)+H$^+$. The specific $n\ell$ values follow Barat and Lichten's correlation rules [42] imposing the conservation of the number of nodes in the radial part of the electronic wave function. This explains the very high density of doubly excited states, and the difficulty to follow them towards the united atom and separated atom limit, respectively.

The first series leading to a pair of excited atoms, *i.e.* the Q_2 $2p\pi_u n\ell\lambda_{g,u}$ states, will generate a $2p$ or $2s$ atom in combination with an $n \geq 2$ atom. From what is written above, the configuration $2p\pi_u 3d\sigma_g$ $^1\Pi_u$ would lead to the formation of H(2p)+H(2p) while $2p\pi_u 2s\sigma_g$ $^1\Pi_u$ would lead to H(2p)+H(2s) (*gerade* states are not discussed here as they are not accessed by single photon transitions).

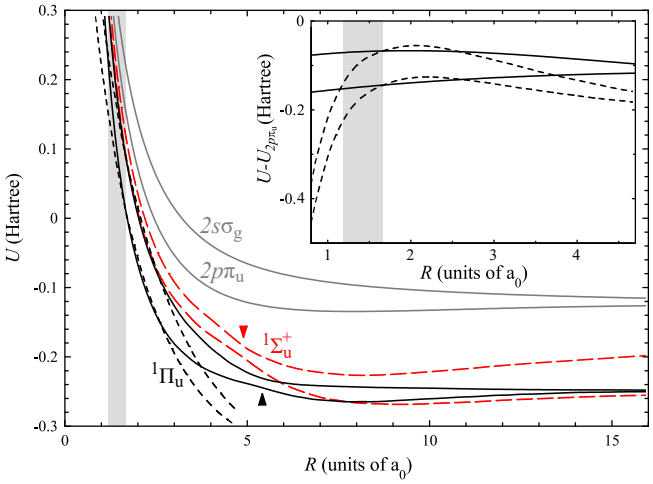

Figure 12. Potential energy curves of the lowest Q_2 $^1\Pi_u$ (full black lines) and $^1\Sigma_u^+$ (dashed red lines) autoionizing states of H_2. Also shown are the Q_2 $^1\Pi_u$ potential curves of Glass-Maujean and Schmoranzer [30] (short dashed black lines), and the potential energy curves of the $2p\pi_u$ $^2\Pi_u$ and $2s\sigma_g$ $^2\Sigma_g^+$ states of H_2^+ (full gray lines). The energy difference between the $^1\Pi_u$ and $^2\Pi_u$ states is shown in the inset. The gray area marks the Franck-Condon region. Arrows point to the avoided crossings (see text).

The corresponding potential energy curves have been computed at numerous instances, the most complete dataset being those computed by Sánchez and Martín [40] (Q_1 and Q_2 states), and by Fernández and Martín [41] (Q_3 and Q_4 states). The first two curves of $^1\Pi_u$ and $^1\Sigma_u^+$ symmetry are plotted in Fig. 12, where we have smoothly connected them to the long-range calculations of Vanne *et al* [43]. The latter predict that Q_2 $^1\Pi_u(1)$ correlates with H(2p)+H(2p), and Q_2 $^1\Pi_u(2)$ and Q_2 $^1\Sigma_u^+(1)$ with H(2s)+H(2p), implying that Q_2 $^1\Sigma_u^+(2)$ correlates with some H(2p)+H(3ℓ) limit. Also plotted are the empirical potential energy curves of Glass-Maujean and Schmoranzer [30] that best fit the observed excitation profile. The latter curves however depart significantly from the expected Rydberg character emerging from a $2p\pi_u$ or $2s\sigma_g$ core, as may be seen in the inset of Fig. 12, where we plot the energy difference between the first two Q_2 $^1\Pi_u$ states of H_2 and the $2p\pi_u$ $^2\Pi_u$ state of H_2^+. This difference should remain nearly constant over the depicted R range, as verified with the curves of Sánchez and Martín [40].

The nearly complete degeneracy of $n\ell$ states requires to follow the dissociation up to large distances where nonadiabatic transitions take place. Such calculations have been performed by Vanne *et al.* [43], Sanz-Vicario *et al.* [36], and Santos *et al.* [44]. A crude diabatization of the long range avoided crossing between Q_2 $^1\Pi_u(1)$ and Q_2 $^1\Pi_u(2)$ curves provides a Landau-Zener transition probability of $\sim 50\%$ at the peak of the H(2p)+H(2p) coincidence signal. Hence both states are likely to contribute evenly. A similar conclusion may be reached when considering the first and second $^1\Sigma_u^+$ curves, *i.e.* that both of them are likely to contribute to H(2p)+H(3ℓ) production.

In order to obtain the excitation profile corresponding to the Q_2 $^1\Pi_u(1)$ and Q_2 $^1\Sigma_u^+(2)$ states (see Fig. 11), we have performed a model calculation of the photodissociation cross section:

$$\sigma_{\rm PD}(\nu) = \frac{2\pi^2\nu}{3c\epsilon_0} | < F(E)|Q_e(R)|\chi_0 > |^2 \qquad (14)$$

where χ_0 is the H_2 vibrational ground state wave function, $Q_e(R)$ the R-dependent dipole matrix element and $F(E)$ is the continuum wave function associated to the dissociative state. In the absence of reliable dipole matrix elements, we have made two simple assumptions: a linear dependence on R, and a constant value. A rapid comparison with the experimental line profile, shown in Fig. 11, favors the linearly dependent matrix element for both symmetries, and further confirms our symmetry assignment, *i.e.* that Q_2 $^1\Pi_u(1)$ and Q_2 $^1\Sigma_u^+(2)$ are the leading contributors to the observed H(2p)+H(2p) and H(2p)+H(3d) signals, respectively. Also shown in Fig. 12 are the excitation curves computed by Glass-Maujean and Schmoranzer [30] with the help of their empirical potential energy curves. One notices that these excitation curves reproduce the peak position but underestimate the width of the excitation profiles. Moreover, it should be noted that the present model only concentrates on the absorption process via the linear dependence of the transition dipole and omits the role of autoionization along the dissociation path and the highly nonadiabatic behavior of the dissociation dynamics, as demonstrated by the time-dependent Schrödinger equation (TDSE) calculations performed by Sanz-Vicario *et al.* [36].

V. ANGULAR CORRELATION FUNCTION

The ACF was obtained following the procedure described in the previous section for each orientation of the polarization axis with respect to the detector interaxis. Three different polarizations were available at the DESIRS synchrotron beamline: vertical, 45° and horizontal[1]. The count rate was measured for these three polarizations, as shown in Fig. 13. The measured ACF is compatible with the previous experimental results [17, 26, 28].

For a meaningful comparison with experiment, the theoretical ACF must be averaged over the detection area and the interaction volume as illustrated in Fig. 1(a). This was evaluated using a Monte Carlo procedure.

In order to describe the angular correlation function, it is useful to follow the sequence of the process. First a H_2 molecule in its ground state $^1\Sigma_g^+$ is excited in the Q_2 $^1\Pi_u(1)$ state. As this electronic state is dissociative, the molecule dissociates in two H(2p) atoms. The selection rules for the emission of two photons in Hund's case (a) impose that the molecule ends up in a $^1\Sigma_u^+$ state, which contradicts the Wigner-Witmer rules [45]. Indeed, only $^1\Sigma_g^+$ and $^3\Sigma_u^+$ are allowed for a homonuclear system dissociating in a pair of S atoms. This inconsistency was lifted by Torizuka *et al* [26] who observed the near-degeneracy of the Q_2 $^1\Pi_u(1)$ and Q_2 $^3\Sigma_u^+(2)$ states at an interatomic distance below 100 a_0, where a_0 is the Bohr radius. Spin-orbit coupling would thus mix those states maximally and modify the decay dynamics that ensues, in particular it would allow for a two-photon decay to the $^3\Sigma_u^+$ ground state. A two-state treatment is adopted by these authors for the sake of simplicity, and found to reproduce the experimental distribution satisfactorily.

However, in order to describe the decay dynamics, one needs to keep in mind that the average time before the emission of the first photon leads to an average distance between the two atoms of 46 μm $= 8.7 \times 10^5$ a_0. This large interatomic distance questions the validity of Hund's case (a) representation which supposes that the atomic $2p_{1/2} - 2p_{3/2}$ splitting (14×10^{-5} eV) is negligible compared to the molecular binding energy, as described by Vanne *et al.* [43]. Instead, the molecular binding energy is negligible compared to the $2p_{1/2} - 2p_{3/2}$ splitting when the interatomic distance is greater than 300 a_0.

[1] The 45° polarization may have contained an unknown fraction of circular polarization.

Hund's case (c) should thus be adopted here, meaning that only Ω ($\Omega = |\tilde{\Omega}|$, $\tilde{\Omega} = \tilde{\Lambda} + \tilde{\Sigma}$, $\tilde{\Lambda}$ and $\tilde{\Sigma}$ being respectively the projection of the molecular electronic orbital momentum and of the electronic spin along the interatomic axis) and overall parity p (*gerade* or *ungerade*) are valid symmetries. As a consequence, the molecule, once dissociated, ends up in a $\Omega_p = 1_u$ state.

One should also take into account the photon detection process. Once the first photon is emitted, as the detectors are situated at less than 3 cm from the excited molecule, this first photon reaches the detector in less than 0.1 ns *i.e.* well before the second photon is emitted.

A simple man's model could be the following: the ground state molecule is initially randomly oriented, then the synchrotron photon excites it in a $^1\Pi_u$ state with a probability $\sin^2\theta_{\varepsilon,R}$ where $\theta_{\varepsilon,R}$ is the angle between the polarization and the interatomic axis. The molecular dissociation can be described under the axial recoil approximation, since the molecular axis turns by less than one degree during the rapid dissociation. The polarization of the recoiling H($2p$) atoms remains only defined in the molecular frame, instead of the laboratory frame, as a result of multiple avoided crossings and spin-orbit coupling among the potential energy curves (PECs). The next assumption of this model is that both atoms will emit light long after the synchrotron electromagnetic field has vanished (after tens of picoseconds). The orbital momentum of the $2p$ orbital has to be projected along the interatomic axis which defines a $2p_{m_l}$ state. As the first photon is detected before the second is emitted, the photon angular emission is independent for each atom. The $2p_0$ orbital emits light with a probability $\sin^2\theta_{\gamma,R}$, while the $2p_{\pm1}$ orbitals emits light with a probability $\cos^2\theta_{\gamma,R}$, where $\theta_{\gamma,R}$ is the angle between the interatomic axis and the Lyman-α propagation axis [46]. It now only remains to determine the orbital momentum projection of the $2p$ orbitals in the molecular frame before they decay. Those are readily obtained by applying the Wigner-Witmer rules [45] and listing all combinations of (m_{l_1}, m_{l_2}) that satisfy the 1_u requirement (see Appendix B, Table I). Adding their contribution incoherently gives the ACF in the molecular frame:

$$\begin{aligned} p_{\mathrm{ACF}}(\theta_{\varepsilon,R},\theta_{\gamma_1,R},\theta_{\gamma_2,R}) &= \sin^2\theta_{\varepsilon,R}\times \\ &\Big[2(\sin^2\theta_{\gamma_1,R}\sin^2\theta_{\gamma_2,R} + \sin^2\theta_{\gamma_2,R}\sin^2\theta_{\gamma_1,R}) \\ &+ 8(\sin^2\theta_{\gamma_1,R}\cos^2\theta_{\gamma_2,R} + \sin^2\theta_{\gamma_2,R}\cos^2\theta_{\gamma_1,R}) \\ &+ 6(\cos^2\theta_{\gamma_1,R}\cos^2\theta_{\gamma_2,R} + \cos^2\theta_{\gamma_2,R}\cos^2\theta_{\gamma_1,R})\Big] \end{aligned} \tag{15}$$

which still has to be averaged over all initial molecular orientations in the laboratory frame.

The present model reproduces the amplitude of the angular modulation seen in the ACF quite satisfactorily, while it does not show the same sensitivity to detector arrangement as the model of Torizuka *et al.* However, the latter explicitly involves a two-photon *ungerade* to *gerade* transition from the H($2p$)+H($2p$) 1_u to the H($1s$)+H($1s$) 1_g state. This surprising assumption rests on the *ungerade* symmetry being imparted to the entangled photon pair, which contradicts the sequential emission and detection of the Lyman-α photons.

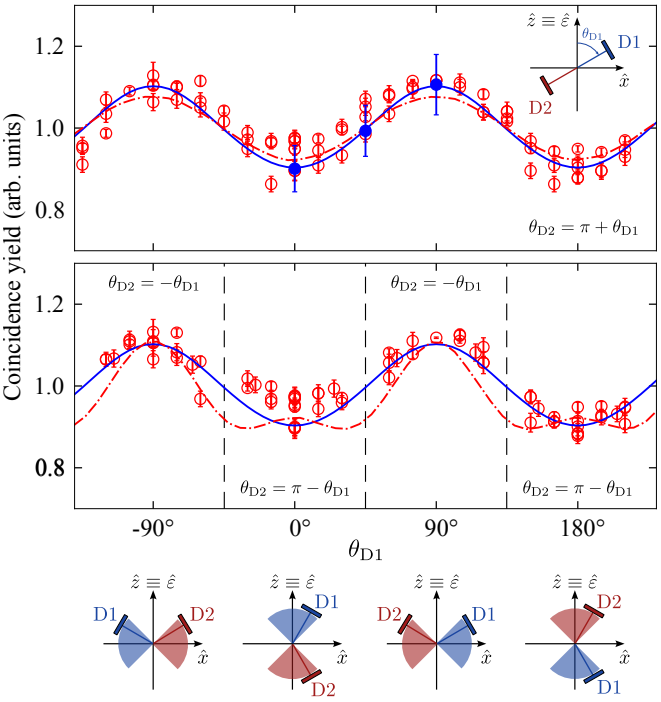

Figure 13. Coincidence yield for different detection geometries and relative orientations of the detectors with respect to the polarization axis given by the angles θ_{D1} and θ_{D2}. Top panel: configuration where the two detectors are facing each other. This configuration corresponds to the measurements performed in this study. All data are averaged over a 0.64 sr solid angle and an interaction length equal to the detector's diameter [17], and scaled for their average to be equal to one. Bottom panel: other detector orientations detailed below the graph. Data are scaled using the same factor as for the top panel. Models from this work and from Torizuka *et al.* [26] are presented in both graphs. Experiment: filled blue circles (this work); open red circles [26]. Theory: dot-dashed red curve [26]; full blue line (this work).

A complete description of the coherent two-photon emission process was offered by Jänkälä *et al.* [16]. This more sophisticated model does not reproduce the ACF in any of the geometries studied, as discussed by Torizuka *et al* [26].

VI. CONCLUSIONS

We have studied the production of pairs of Lyman-α photons upon XUV excitation of H_2. By time referencing the fluorescence photon detection to the synchrotron light pulse, we were able to extract the partial cross sections for the H($2p$) + H($2p$) and H($2p$) + H(3ℓ) channels.

A pressure dependence analysis allowed us to isolate them from accidental coincidences. Close examination

of the doubly excited states lying in the Franck-Condon window confirms the prior assignment of the H($2p$) + H($2p$) channel to the $Q_2\ ^1\Pi_u(1)$ state.

The angular dependence of the two-photon detection probability with respect to the polarization axis was verified to match earlier measurements. A simple model is proposed to account for the spin-orbit mixing taking place at large distances, which assumes a transition from Hund's case (a) to Hund's case (c). The main consequence of that crude treatment is that the final state is solely of 1_u character,as opposed to the model of Torizuka *et al.*, which predicts that both $^1\Sigma_g^+$ and $^3\Sigma_u^+$ symmetries are populated.

At this stage, a significant increase of the measurement statistics would allow to perform measurements more sensitive to entanglement.

For the specific case of the measurement of the decay dynamics, lowering the pressure while increasing the coincidence integration window should make possible a better separation of the different deexcitation channels. This selection can also be achieved by varying the excitation wavelength.

For angle resolved measurements, polarization sensitive detectors should be used while increasing the distance between them. Similarly, while carrying out the measurement of the ACF over the whole range of angles between the polarization and detector axis, it would be interesting to concentrate the measurements around 45° where differences between the various theoretical approaches are the most significant.

Additionally, applying the same experimental procedure to hydrogen deuteride should allow, by breaking the symmetry, to lift ambiguities between the different theories, as was recently done by Hosaka *et al.* [37].

These improvements, impacting both temporal and angular selectivity, will lead to a more decisive conclusion concerning the influence of entanglement on the deexcitation process of doubly excited H_2.

ACKNOWLEDGEMENTS

The authors would like to thank Yann Mairesse, Laurent Nahon and Nelson de Oliveira for their help and support. They also thank Jean-Michel Raimond for valuable discussions regarding the applicability of the superradiance model and Bernard Pons for discussions concerning the theoretical models. This work was performed at the SOLEIL synchrotron under Proposal No. 20140225. We acknowledge SOLEIL for provision of synchrotron radiation facilities and the DESIRS beamline team for their assistance. This work was supported by the Fonds de la Recherche Scientifique - FNRS under IISN grant No. 4.4504.10. X.U. is a Senior Research Associate of the Fonds de la Recherche Scientifique – FNRS.

Appendix A: Effects of the coincidence window on the measured decay dynamics

1. General formulae

This section details how the measured decay dynamics is affected by the coincidence window length. This description is given under the following assumption: the coincident decay dynamics is generated by two independent random distributions $p(t_1 = t)$ and $p(t_2 = t)$ where t is bounded between $t_{\min}$ and $t_{\max}$, defining the coincidence window duration as $\Delta t = t_{\max} - t_{\min}$. Each distribution is associated with a decay process. They are not necessarily identical. Each event generates a combination of (t_1, t_2), those are detected by two detectors D1 and D2, leading to the corresponding event $(t_{\mathrm{D1}}, t_{\mathrm{D2}})$. But the fact that, for each event, the probabilities are $p(t_1 = t_{\mathrm{D1}}) = p(t_1 = t_{\mathrm{D2}}) = 0.5$, leads to the impossibility to directly extract the distributions $p(t_1 = t)$ and $p(t_2 = t)$ from $p(t_{\mathrm{D1}} = t)$ and $p(t_{\mathrm{D2}} = t)$.

In order to circumvent this problem, the decay dynamics is studied using the sorted time distribution

$$t_f = \min(t_1, t_2) = \min(t_{\mathrm{D1}}, t_{\mathrm{D2}}) \tag{A1}$$
$$t_s = \max(t_1, t_2) = \max(t_{\mathrm{D1}}, t_{\mathrm{D2}}) \tag{A2}$$

where t_f is the first photon detection event and t_s is second. One can note that (t_f, t_s) do not depend on whether $t_{\mathrm{D1}} = t_1, t_{\mathrm{D2}} = t_2$ or $t_{\mathrm{D1}} = t_2, t_{\mathrm{D2}} = t_1$. This means that the experimental distribution (t_f, t_s) measured using a subset of $(t_{\mathrm{D1}}, t_{\mathrm{D2}})$ is identical to the theoretical distribution predicted by the computation of a subset of (t_1, t_2). Therefore, the probability density function $p(t_f = t)$ and $p(t_s = t)$ can be obtained using law of total probability:

$$p(A) = \sum_i p(A|B_i)p(B_i) \tag{A3}$$

applied to (t_1, t_2), which leads to

$$\begin{aligned} p(t_f = t) =& p(t_f = t|t_1 < t_2)p(t_1 < t_2) \\ &+ p(t_f = t|t_2 < t_1)p(t_2 < t_1) \end{aligned} \tag{A4}$$
$$\begin{aligned} p(t_s = t) =& p(t_s = t|t_1 > t_2)p(t_1 > t_2) \\ &+ p(t_s = t|t_2 > t_1)p(t_2 > t_1) \end{aligned} \tag{A5}$$

where $p(t_f = t|t_1 < t_2)$ is the probability to measure t_f at a time t if the event satisfies the condition $t_1 < t_2$. Then $t_f = t_1$ if this condition is satisfied, $t_f = t_2$ otherwise. The previous equation is then:

$$\begin{aligned} p(t_f = t) =& p(t_1 = t|t_1 < t_2)p(t_1 < t_2) \\ &+ p(t_2 = t|t_2 < t_1)p(t_2 < t_1) \\ p(t_s = t) =& p(t_1 = t|t_1 > t_2)p(t_1 > t_2) \\ &+ p(t_2 = t|t_2 > t_1)p(t_2 > t_1) \end{aligned}$$

The terms $p(t_i = t|t_i < t_j)$ are not easy to compute, but can easily be transformed using Bayes' theorem

$$p(A|B) = \frac{p(B|A)p(A)}{p(B)} \tag{A6}$$

which leads to

$$\begin{aligned} p(t_f = t) =& p(t_1 = t)p(t_1 < t_2|t_1 = t) \\ &+ p(t_2 = t)p(t_2 < t_1|t_2 = t) \\ p(t_s = t) =& p(t_1 = t)p(t_1 > t_2|t_1 = t) \\ &+ p(t_2 = t)p(t_2 > t_1|t_2 = t) \end{aligned}$$

As writing $p(t_1 < t_2|t_1 = t)$ is equivalent to say *the probability that the event t_1 is smaller than an element of the t_2 distribution if the event t_1 is equal to the value t*, which means that *the probability that an element of the t_2 distribution is greater than the value t*, then $p(t_1 < t_2|t_1 = t) = p(t_2 > t)$. When the previous equations take into account this argument, they are rewritten as

$$\begin{aligned} p(t_f = t) =& p(t_1 = t)p(t_2 > t) \\ &+ p(t_2 = t)p(t_1 > t) \\ p(t_s = t) =& p(t_1 = t)p(t_2 < t) \\ &+ p(t_2 = t)p(t_1 < t) \end{aligned}$$

Then, since the probability $p(t_i < t)$ is defined by

$$p(t_i < t) = \int_{t_{\min}}^{t} \mathrm{d}t' \; p(t_i = t') \tag{A7}$$

and $p(t_i > t)$ is defined by

$$p(t_i > t) = \int_{t}^{t_{\max}} \mathrm{d}t' \; p(t_i = t') \tag{A8}$$

The previous equation is written as

$$\begin{aligned} p(t_f = t) =& p(t_1 = t) \int_{t}^{t_{\max}} \mathrm{d}t' \; p(t_2 = t') \\ &+ p(t_2 = t) \int_{t}^{t_{\max}} \mathrm{d}t' \; p(t_1 = t') \qquad \text{(A9)} \\ p(t_s = t) =& p(t_1 = t) \int_{t_{\min}}^{t} \mathrm{d}t' \; p(t_2 = t') \\ &+ p(t_2 = t) \int_{t_{\min}}^{t} \mathrm{d}t' \; p(t_1 = t') \qquad \text{(A10)} \end{aligned}$$

These equations give the emission rates $p_f(t) = p(t_f = t)$ and $p_s(t) = p(t_s = t)$ of the first and second photon over time t. However, the experimental emission rate depends on the time binning of the events. The method used to bypass this problem is to integrate over all the events that happened before the time t :

$$\begin{aligned} P_f(t) =& p(t_f < t) \\ =& \int_{t_{\min}}^{t} \mathrm{d}t' \; p(t_f = t') \\ =& \int_{t_{\min}}^{t} \mathrm{d}t' \; p(t_1 = t') \int_{t'}^{t_{\max}} \mathrm{d}t'' \; p(t_2 = t'') \\ &+ \int_{t_{\min}}^{t} \mathrm{d}t' \; p(t_2 = t') \int_{t'}^{t_{\max}} \mathrm{d}t'' \; p(t_1 = t'') \end{aligned} \tag{A11}$$

$$\begin{aligned} P_s(t) =& p(t_s < t) \\ =& \int_{t_{\min}}^{t} \mathrm{d}t' \; p(t_s = t') \\ =& \int_{t_{\min}}^{t} \mathrm{d}t' \; p(t_1 = t') \int_{t_{\min}}^{t'} \mathrm{d}t'' \; p(t_2 = t'') \\ &+ \int_{t_{\min}}^{t} \mathrm{d}t' \; p(t_2 = t') \int_{t_{\min}}^{t'} \mathrm{d}t'' \; p(t_1 = t'') \end{aligned} \tag{A12}$$

This general formula depends only on the time distribution of t_1 and t_2.

2. Emission rate normalization

If the theoretical distribution (t_1, t_2) is not initially bounded between $t_{\min}$ and $t_{\max}$, there are events falling outside the coincidence window. They cannot be measured. It means that, for $t_1 \notin [t_{\min}, t_{\max}]$ a random event from the distribution t_2 occurs. As t_2 is independent of t_1, the single event appearing at t_2 is lost with a probability $p(t_2 = t)$. This means that $p(t_1 = t)$ and $p(t_2 = t)$ can be normalized independently:

$$\tilde{p}(t_1 = t) = \frac{p(t_1 = t)}{\int_{t_{\min}}^{t_{\max}} \mathrm{d}t' \; p(t_1 = t')} \tag{A13}$$

$$\tilde{p}(t_2 = t) = \frac{p(t_2 = t)}{\int_{t_{\min}}^{t_{\max}} \mathrm{d}t' \; p(t_2 = t')} \tag{A14}$$

where the tildes indicate normalized values with $t_{\max} - t_{\min} = \Delta t$.

This normalization must be applied to t_1 and t_2 not t_f and t_s because t_f and t_s are not independent. This assertion can be explained as follows: If a second photon is emitted at time T_s after $t_{\max}$, the coincident event cannot be detected. It is therefore needed to remove that event from the t_f distribution. But this event cannot be random, it must satisfy $T_f < T_s$. This changes the shape of the t_f distribution. Which means that the t_f and t_s distributions cannot be normalized independently. However, it is easy to verify that if $p(t_1 = t)$ and $p(t_2 = t)$ are normalized, then $p(t_f = t)$ and $p(t_s = t)$ are also normalized.

This normalization method is also used to extract the number of coincident events which physically happened

but cannot be measured because either t_1 or t_2 is outside the interval $[t_{\min}, t_{\max}]$.

The physics of the decay dynamics is bounded between $t_{\min} = 0$ and $t_{\max} = \infty$. The experimental setup records events between $t_{\min} = 0$ and $t_{\max} = \Delta t$. It means that the experiment cannot measure any event where $t_s > \Delta t$ (t_f is not taken into account because if $t_s < \Delta t$ then $t_f < \Delta t$). If we note

$$\tilde{P}_s(t) = \int_0^t \mathrm{d}t'\ \tilde{p}(t_1 = t') \int_0^{t'} \mathrm{d}t''\ \tilde{p}(t_2 = t'') + \int_0^t \mathrm{d}t'\ \tilde{p}(t_2 = t') \int_0^{t'} \mathrm{d}t''\ \tilde{p}(t_1 = t''), \quad \text{(A15)}$$

the number of events physically produced N_{all} is linked to the number of events effectively measured N_{meas} by

$$N_{all} = N_{meas} \frac{\tilde{P}_s(\Delta t)}{P_s(\Delta t)}, \quad \text{(A16)}$$

where $\tilde{P}_s(\Delta t)$ is equal to 1 as a result of the normalization procedure.

3. Application to doubly excited H_2

The following cases use the normalized distribution $\tilde{p}(t_1 = t)$ and $\tilde{p}(t_2 = t)$. The time bounds are $t_{\min} = 0$ and $t_{\max} = \Delta t$.

The normalized distributions considered are:

- The single Ly$_\alpha$ emission process from an atom initially in the $2p$ state

$$\tilde{p}^{2p}(t_i = t) = \frac{\Gamma_{2p} e^{-\Gamma_{2p} t}}{1 - e^{-\Gamma_{2p}\Delta t}}$$

where $\Gamma_{2p} = \Gamma_{1s \leftarrow 2p}$ is the decay rate.

- The Ly$_\alpha$ emission is coming from an atom initially in the 3ℓ state, where $\ell = s, d$. The atom emits initially a Hα photon, then a Ly$_\alpha$ photon. Only the Ly$_\alpha$ photon is detected. This distribution is obtained by solving:

$$\begin{aligned} \dot{n}_{3\ell}(t) &= -\Gamma_{3\ell} n_{3\ell}(t) \\ \dot{n}_{2p}(t) &= \Gamma_{3\ell} n_{3\ell}(t) - \Gamma_{2p} n_{2p}(t) \\ \dot{n}_{1s}(t) &= \Gamma_{2p} n_{2p}(t) \end{aligned}$$

where $n_{3\ell}(0) = 1$, $n_{2p}(0) = 0$, $n_{1s}(0) = 0$ and $\Gamma_{3\ell} = \Gamma_{2p \leftarrow 3\ell}$. Then

$$\begin{aligned} \tilde{p}^{3\ell}(t_i = t) =& \dot{n}_{1s}(t) \\ =& \frac{\Gamma_{2p}\Gamma_{3\ell}\left(e^{-\Gamma_{3\ell} t} - e^{-\Gamma_{2p} t}\right)}{\Gamma_{2p}\left(1 - e^{-\Gamma_{3\ell}\Delta t}\right) - \Gamma_{3\ell}\left(1 - e^{-\Gamma_{2p}\Delta t}\right)} \end{aligned}$$

- A random background process, independent of the synchrotron radiation (*e.g.* dark counts of MCP detectors). This process is uniform

$$\tilde{p}^{BG}(t_i = t) = 1/\Delta t$$

- Due to the transmission window of MgF_2 being limited to 110 nm, the Ly$_\beta$ photon, resulting from the deexcitation of an atom initially in the $3p$ state cannot be detected in the present experiment.

Using these formulae, the integrated decay rates are for the $2p - 2p$ coincident distribution:

$$\begin{cases} \tilde{P}_f^{2p-2p}(t) &= \frac{\left(1-e^{-2\Gamma_{2p} t}\right) - 2e^{-\Gamma_{2p}\Delta t}\left(1-e^{-\Gamma_{2p} t}\right)}{\left(1-e^{-\Gamma_{2p}\Delta t}\right)^2} \\ \tilde{P}_s^{2p-2p}(t) &= \frac{\left(1-e^{-\Gamma_{2p} t}\right)^2}{\left(1-e^{-\Gamma_{2p}\Delta t}\right)^2} \end{cases} \quad \text{(A17)}$$

which gives, when $t_{\max} = \infty$:

$$\begin{cases} P_f^{2p-2p}(t) &= \left(1 - e^{-2\Gamma_{2p} t}\right) \\ P_s^{2p-2p}(t) &= \left(1 - e^{-\Gamma_{2p} t}\right)^2 \end{cases} \quad \text{(A18)}$$

whose derivative leads to Eq. (2) and (3) in the main text.

For the $2p - 3\ell$ coincidences, the distributions are:

$$\begin{cases} \tilde{P}_f^{2p-3\ell}(t) = & \Big[(\Gamma_{3\ell} - \Gamma_{2p})(1 - e^{-\Gamma_{2p}\Delta t}) - (\Gamma_{3\ell} e^{-\Gamma_{2p}\Delta t} - \Gamma_{2p} e^{-\Gamma_{3\ell}\Delta t})(1 - e^{-\Gamma_{2p} t}) \\ & \quad -(\Gamma_{3\ell} e^{-\Gamma_{2p} t} - \Gamma_{2p} e^{-\Gamma_{3\ell} t})(e^{-\Gamma_{2p} t} - e^{-\Gamma_{2p}\Delta t})\Big] \\ & \quad \times \Big[(1 - e^{-\Gamma_{2p}\Delta t}) \times \left(\Gamma_{3\ell}(1 - e^{-\Gamma_{2p}\Delta t}) - \Gamma_{2p}(1 - e^{-\Gamma_{3\ell}\Delta t})\right)\Big]^{-1} \\ \tilde{P}_s^{2p-3\ell}(t) = & \Big[(1 - e^{-\Gamma_{2p} t}) \times \left(\Gamma_{3\ell}(1 - e^{-\Gamma_{2p} t}) - \Gamma_{2p}(1 - e^{-\Gamma_{3\ell} t})\right)\Big] \\ & \quad \times \Big[(1 - e^{-\Gamma_{2p}\Delta t}) \times \left(\Gamma_{3\ell}(1 - e^{-\Gamma_{2p}\Delta t}) - \Gamma_{2p}(1 - e^{-\Gamma_{3\ell}\Delta t})\right)\Big]^{-1} \end{cases} \quad \text{(A19)}$$

which gives, when $t_{\max} = \infty$:

$$\begin{cases} P_f^{2p-3\ell}(t) = & \frac{(\Gamma_{3\ell} - \Gamma_{2p}) - \left[\Gamma_{3\ell} e^{-\Gamma_{2p} t} - \Gamma_{2p} e^{-\Gamma_{3\ell} t}\right] e^{-\Gamma_{2p} t}}{\Gamma_{3\ell} - \Gamma_{2p}} \\ P_s^{2p-3\ell}(t) = & \frac{(1 - e^{-\Gamma_{2p} t})\left[\Gamma_{3\ell}(1 - e^{-\Gamma_{2p} t}) - \Gamma_{2p}(1 - e^{-\Gamma_{3\ell} t})\right]}{\Gamma_{3\ell} - \Gamma_{2p}} \end{cases} \quad \text{(A20)}$$

whose derivative leads to Eqs. (7) and (8) in the main text.

The fact that there is nearly no coincident background without the synchrotron radiation does not mean that there is no background process. The coincident background distribution is the following:

$$\begin{cases} \tilde{P}_f^{2p-BG}(t) &= \frac{\Delta t+(t-\Delta t)e^{-t/\tau_{2p}}-te^{-\Delta t/\tau_{2p}}}{\Delta t\left(1-e^{-\Delta t/\tau_{2p}}\right)} \\ \tilde{P}_s^{2p-BG}(t) &= \frac{t\left(1-e^{-t/\tau_{2p}}\right)}{\Delta t\left(1-e^{-\Delta t/\tau_{2p}}\right)} \end{cases} \tag{A21}$$

$$\begin{cases} \tilde{P}_f^{3\ell-BG}(t) = \\ \quad \left[(\Delta t-t)(\Gamma_{3\ell}e^{-\Gamma_{2p}t}-\Gamma_{2p}e^{-\Gamma_{3\ell}t})\right. \\ \quad \left.+\Gamma_{3\ell}(te^{-\Gamma_{2p}\Delta t}-\Delta t)-\Gamma_{2p}(te^{-\Gamma_{3\ell}\Delta t}-\Delta t)\right] \\ \quad \times\left[\Delta t(\Gamma_{3\ell}(e^{-\Gamma_{2p}\Delta t}-1)-\Gamma_{2p}(e^{-\Gamma_{3\ell}\Delta t}-1))\right]^{-1} \\ \tilde{P}_s^{3\ell-BG}(t) = \\ \quad \left[t\left(\Gamma_{3\ell}(e^{-\Gamma_{2p}t}-1)-\Gamma_{2p}(e^{-\Gamma_{3\ell}t}-1)\right)\right] \\ \quad \times\left[\Delta t(\Gamma_{3\ell}(e^{-\Gamma_{2p}\Delta t}-1)-\Gamma_{2p}(e^{-\Gamma_{3\ell}\Delta t}-1))\right]^{-1} \end{cases} \tag{A22}$$

$$\begin{cases} \tilde{P}_f^{BG-BG}(t) &= \frac{2t\Delta t-t^2}{\Delta t^2} \\ \tilde{P}_s^{BG-BG}(t) &= \frac{t^2}{\Delta t^2} \end{cases} \tag{A23}$$

4. Spontaneous decay direct derivation

The differential equations corresponding to the radiative cascade of Figs. 4 and 7 are:

$$\dot{n}_{2p3\ell} = -\Gamma_{3\ell}n_{2p3\ell}-\Gamma_{2p}n_{2p3\ell} \tag{A24}$$
$$\dot{n}_{2p2p} = +\Gamma_{3\ell}n_{2p3\ell}-\Gamma_{2p}n_{2p2p}-\Gamma_{2p}n_{2p2p} \tag{A25}$$
$$\dot{n}_{2p1s} = +\Gamma_{2p}n_{2p2p}-\Gamma_{2p}n_{2p1s} \tag{A26}$$
$$\dot{n}_{1s3\ell} = +\Gamma_{2p}n_{2p3\ell}-\Gamma_{3\ell}n_{1s3\ell} \tag{A27}$$
$$\dot{n}_{1s2p} = +\Gamma_{2p}n_{2p2p}+\Gamma_{3\ell}n_{1s3\ell}-\Gamma_{2p}n_{1s2p} \tag{A28}$$
$$\dot{n}_{1s1s} = +\Gamma_{2p}n_{2p1s}+\Gamma_{2p}n_{1s2p} \tag{A29}$$

where the n correspond to the population of the various states.

The emission rates are defined as

$$\begin{cases} p_f &= -\dot{n}_{2p3\ell}-\dot{n}_{2p2p} \\ p_s &= \dot{n}_{1s1s} \end{cases} \tag{A30}$$

where $(p_f^{\mathrm{SP},2p}, p_s^{\mathrm{SP},2p})$ are the solution of equations (A24)–(A29) with the atoms initially in the $(2p,2p)$ state and $(p_f^{\mathrm{SP},3\ell}, p_s^{\mathrm{SP},3\ell})$ are the solution of these equations when the atoms are initially in the $(2p,3\ell)$ state.

5. Why the $2p-3s$ state is not included in the decay curve fits

Those distributions should be included in the fit. However, when Δt is small compared to $1/\Gamma_{3\ell}$, the exponential decay is close to linear in the recorded time window (Fig. 14). Therefore, the $2p-BG$ distribution is similar to the $2p-3s$ distribution for the coincidence windows used during the experiment (30 ns and 60 ns). This applies for $2p-3d$ only when $\Delta t < 15$ ns.

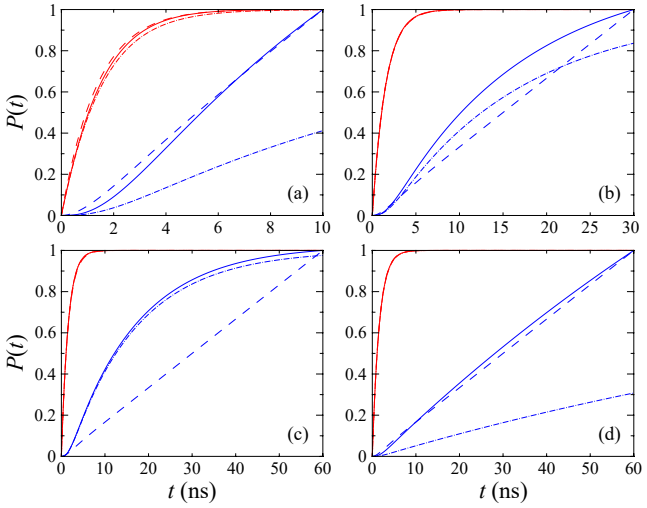

Figure 14. Coincident integrated decay rate for various distributions. First photon P_f: red; second photon P_s: blue. Full lines: $2p-3\ell$, reduced coincidence window $t_{max}=\Delta t$; Dashed-dotted lines: $2p-3\ell$, infinite coincidence window $t_{max}=\infty$; Dashed lines: $2p-BG$, reduced coincident window. Top left (a): $2p-3d$, $\Delta t=10$ ns; Top right (b): $2p-3d$, $\Delta t=30$ ns; Bottom left (c): $2p-3d$, $\Delta t=60$ ns; Bottom right (d): $2p-3s$, $\Delta t=60$ ns.

Appendix B: Non coherent ACF in the molecular frame

At large internuclear distance, we make the assumption that all states of 1_u symmetry are statistically populated as a result of spin-orbit coupling and near degeneracy of all states correlated to $\mathrm{H}(2p)+\mathrm{H}(n=2)$ pairs, among them the Q_2 $^1\Pi_u(1)$ state. Therefore, it cannot be solely defined by the $2p_{1/2}$ or $2p_{3/2}$ states of the separated atoms. Instead, one has to build the 1_u wavefunction from the $(2p,2p)$ asymptotic case without initially defining J. One way to do so is to detail the atomic wavefunctions from the Wigner-Witmer rules applied to Hund's case (a) and then to determine which substate is associated to a 1_u state in Hund's case (c) framework.

The ^2P_u – ^2P_u combination generates the following symmetries, the number of states of each symmetry being given here in parentheses[45]: $^1\Sigma_g^+(2)$, $^1\Sigma_u^-(1)$, $^3\Sigma_g^-(1)$, $^3\Sigma_u^+(2)$, $^1\Pi_g(1)$, $^1\Pi_u(1)$, $^3\Pi_g(1)$, $^3\Pi_u(1)$, $^1\Delta_g(1)$, and $^3\Delta_u(1)$.

Each of these states is weighted by its multiplicity (due to S and Λ). Then, by listing all the m_l and m_s of each atom, one should assign each of these combinations to a (combination of) Hund's case (a) symmetry in order ensure that the state is an *ungerade* state. It only remains

to sum over all the combinations, and add them:

$$\sin^2(\theta_{\gamma_1,R})\sin^2(\theta_{\gamma_2,R})+\sin^2(\theta_{\gamma_2,R})\sin^2(\theta_{\gamma_1,R}) \quad \text{if } m_l(1)=0 \text{ and } m_l(2)=0 \tag{B1}$$

$$\sin^2(\theta_{\gamma_1,R})\cos^2(\theta_{\gamma_2,R})+\sin^2(\theta_{\gamma_2,R})\cos^2(\theta_{\gamma_1,R}) \quad \begin{cases} \text{if } m_l(1)=\pm1 \text{ and } m_l(2)=0 \\ \text{or } m_l(1)=0 \text{ and } m_l(2)=\pm1 \end{cases} \tag{B2}$$

$$\cos^2(\theta_{\gamma_1,R})\cos^2(\theta_{\gamma_2,R})+\cos^2(\theta_{\gamma_2,R})\cos^2(\theta_{\gamma_1,R}) \quad \text{if } m_l(1)=\pm1 \text{ and } m_l(2)=\pm1. \tag{B3}$$

for each term which satisfies $\tilde{\Omega}=\pm1$ for an *ungerade* state.

Once this is done (see Table I), one obtains the ACF in the molecular frame:

$$\begin{aligned} p_{\mathrm{ACF}}(\theta_{\varepsilon,R},\theta_{\gamma_1,R},\theta_{\gamma_2,R}) &= \sin^2\theta_{\varepsilon,R}\times \\ &\big[2(\sin^2\theta_{\gamma_1,R}\sin^2\theta_{\gamma_2,R}+\sin^2\theta_{\gamma_2,R}\sin^2\theta_{\gamma_1,R}) \\ &+8(\sin^2\theta_{\gamma_1,R}\cos^2\theta_{\gamma_2,R}+\sin^2\theta_{\gamma_2,R}\cos^2\theta_{\gamma_1,R}) \\ &+6(\cos^2\theta_{\gamma_1,R}\cos^2\theta_{\gamma_2,R}+\cos^2\theta_{\gamma_2,R}\cos^2\theta_{\gamma_1,R})\big] \end{aligned} \tag{B4}$$

m_{l_1}	m_{s_1}	m_{l_2}	m_{s_2}	$\tilde{\Lambda}$	$\tilde{\Sigma}$	$\tilde{\Omega}$	Hund's case (a)
+1	+1/2	+1	+1/2	+2	+1	+3	$^3\Delta_u$
+1	+1/2	+1	-1/2	+2	0	+2	$^3\Delta_u$
+1	-1/2	+1	+1/2	+2	0	+2	$^3\Delta_u$
+1	**-1/2**	**+1**	**-1/2**	**+2**	**-1**	**+1**	$\mathbf{^3\Delta_u}$
-1	**+1/2**	**-1**	**+1/2**	**-2**	**+1**	**-1**	$\mathbf{^3\Delta_u}$
-1	+1/2	-1	-1/2	-2	0	-2	$^3\Delta_u$
-1	-1/2	-1	+1/2	-2	0	-2	$^3\Delta_u$
-1	-1/2	-1	-1/2	-2	-1	-3	$^3\Delta_u$
+1	+1/2	0	+1/2	+1	+1	+2	$^3\Pi_u$
+1	**+1/2**	**0**	**-1/2**	**+1**	**0**	**+1**	$\mathbf{^3\Pi_u}, ^1\mathbf{\Pi_u}$
+1	**-1/2**	**0**	**+1/2**	**+1**	**0**	**+1**	$\mathbf{^3\Pi_u}, ^1\mathbf{\Pi_u}$
+1	-1/2	0	-1/2	+1	-1	0	$^3\Pi_u$
0	+1/2	+1	+1/2	+1	+1	+2	$^3\Pi_u$
0	**+1/2**	**+1**	**-1/2**	**+1**	**0**	**+1**	$\mathbf{^3\Pi_u}, ^1\mathbf{\Pi_u}$
0	**-1/2**	**+1**	**+1/2**	**+1**	**0**	**+1**	$\mathbf{^3\Pi_u}, ^1\mathbf{\Pi_u}$
0	-1/2	+1	-1/2	+1	-1	0	$^3\Pi_u$
-1	+1/2	0	+1/2	-1	+1	0	$^3\Pi_u$
-1	**+1/2**	**0**	**-1/2**	**-1**	**0**	**-1**	$\mathbf{^3\Pi_u}, ^1\mathbf{\Pi_u}$
-1	**-1/2**	**0**	**+1/2**	**-1**	**0**	**-1**	$\mathbf{^3\Pi_u}, ^1\mathbf{\Pi_u}$
-1	-1/2	0	-1/2	-1	-1	-2	$^3\Pi_u$
0	+1/2	-1	+1/2	-1	+1	0	$^3\Pi_u$
0	**+1/2**	**-1**	**-1/2**	**-1**	**0**	**-1**	$\mathbf{^3\Pi_u}, ^1\mathbf{\Pi_u}$
0	**-1/2**	**-1**	**+1/2**	**-1**	**0**	**-1**	$\mathbf{^3\Pi_u}, ^1\mathbf{\Pi_u}$
0	-1/2	-1	-1/2	-1	-1	-2	$^3\Pi_u$
0	**+1/2**	**0**	**+1/2**	**0**	**+1**	**+1**	$\mathbf{^3\Sigma_u^+}$
0	+1/2	0	-1/2	0	0	0	$^3\Sigma_u^+$
0	-1/2	0	+1/2	0	0	0	$^3\Sigma_u^+$
0	**-1/2**	**0**	**-1/2**	**0**	**-1**	**-1**	$\mathbf{^3\Sigma_u^+}$
+1	**+1/2**	**-1**	**+1/2**	**0**	**+1**	**+1**	$\mathbf{^3\Sigma_u^+}$
+1	+1/2	-1	-1/2	0	0	0	$^3\Sigma_u^+, ^1\Sigma_u^-$
+1	-1/2	-1	+1/2	0	0	0	$^3\Sigma_u^+, ^1\Sigma_u^-$
+1	**-1/2**	**-1**	**-1/2**	**0**	**-1**	**-1**	$\mathbf{^3\Sigma_u^+}$
-1	**+1/2**	**+1**	**+1/2**	**0**	**+1**	**+1**	$\mathbf{^3\Sigma_u^+}$
-1	+1/2	+1	-1/2	0	0	0	$^3\Sigma_u^+, ^1\Sigma_u^-$
-1	-1/2	+1	+1/2	0	0	0	$^3\Sigma_u^+, ^1\Sigma_u^-$
-1	**-1/2**	**+1**	**-1/2**	**0**	**-1**	**-1**	$\mathbf{^3\Sigma_u^+}$

Table I. Combination of all m_l and m_s values, associated with Hund's case (a) and (c). Only the *ungerade* symmetries are displayed. The rows highlighted in bold face ($\tilde{\Omega}=\pm1$) are the ones contributing to the emission.

[1] D. Bohm, *Quantum theory* (Prentice-Hall, Englewood Cliffs, N.J., 1951).
[2] S. J. Freedman and J. F. Clauser, Phys. Rev. Lett. **28**, 938 (1972).
[3] A. Aspect, J. Dalibard, and G. Roger, Phys. Rev. Lett. **49**, 1804 (1982).
[4] J.-W. Pan, D. Bouwmeester, H. Weinfurter, and A. Zeilinger, Phys. Rev. Lett. **80**, 3891 (1998).
[5] J. Robert, C. Miniatura, S. L. Boiteux, J. Reinhardt, V. Bocvarski, and J. Baudon, Europhysics Letters (EPL) **16**, 29 (1991).
[6] C. Miniatura, J. Robert, O. Gorceix, V. Lorent, S. Le Boiteux, J. Reinhardt, and J. Baudon, Phys. Rev. Lett. **69**, 261 (1992).
[7] E. S. Fry and T. Walther (Academic Press, 2000) pp. 1–27.
[8] T. Walther and E. S. Fry, Journal of Optics B: Quantum and Semiclassical Optics **4**, S376 (2002).
[9] J. Koperski, M. Strojecki, M. Krośnicki, and T. Urbańczyk, The Journal of Physical Chemistry A **115**, 6851 (2011), pMID: 21410152, https://doi.org/10.1021/jp1112922.
[10] S. Y. Grebenshchikov and D. Picconi, Chemical Physics **515**, 60 (2018), ultrafast Photoinduced Processes in Polyatomic Molecules:Electronic Structure, Dynamics and Spectroscopy (Dedicated to Wolfgang Domcke on the occasion of his 70th birthday).
[11] F. Borselli, M. Maiwöger, T. Zhang, P. Haslinger, V. Mukherjee, A. Negretti, S. Montangero, T. Calarco, I. Mazets, M. Bonneau, and J. Schmiedmayer, Phys. Rev. Lett. **126**, 083603 (2021).
[12] S. Arai, T. Kamosaki, M. Ukai, K. Shinsaka, Y. Hatano, Y. Ito, H. Koizumi, A. Yagishita, K. Ito, and K. Tanaka, The Journal of Chemical Physics **88**, 3016 (1988), https://doi.org/10.1063/1.453943.
[13] T. Odagiri, T. Tanabe, and N. Kouchi, Journal of Physics: Conference Series **388**, 012024 (2012).
[14] T. Tanabe, T. Odagiri, M. Nakano, I. H. Suzuki, and N. Kouchi, Phys. Rev. Lett. **103**, 173002 (2009).
[15] T. Tanabe, T. Odagiri, M. Nakano, Y. Kumagai, I. H. Suzuki, M. Kitajima, and N. Kouchi, Phys. Rev. A **82**, 040101 (2010).
[16] K. Jänkälä, P. V. Demekhin, S. Heinäsmäki, I. Haar, R. Hentges, and A. Ehresmann, Journal of Physics B: Atomic, Molecular and Optical Physics **43**, 065104 (2010).
[17] Y. Nakanishi, K. Hosaka, R. Kougo, T. Odagiri, M. Nakano, Y. Kumagai, K. Shiino, M. Kitajima, and N. Kouchi, Phys. Rev. A **90**, 043405 (2014).
[18] P. Sancho, Phys. Rev. A **95**, 032116 (2017).
[19] H. Miyagi, A. Ichimura, and N. Kouchi, Journal of Physics B: Atomic, Molecular and Optical Physics **40**, 617 (2007).
[20] M.-E. Couprie, L. S. Nadolski, R. Nagaoka, P. Brunelle, A. Loulergue, M. A. Tordeux, J. F. Lamarre, and A. Nadji, Synchrotron Radiation News **26**, 14 (2013), https://doi.org/10.1080/08940886.2013.791210.
[21] N. R. Daly, Review of Scientific Instruments **31**, 264 (1960), https://doi.org/10.1063/1.1716953.
[22] T. Odagiri, M. Murata, M. Kato, and N. Kouchi, Journal of Physics B: Atomic, Molecular and Optical Physics **37**, 3909 (2004).
[23] P. Sancho and L. Plaja, Phys. Rev. A **83**, 066101 (2011).
[24] M. Gross and S. Haroche, Physics Reports **93**, 301 (1982).
[25] NIST Atomic Spectra Database, http://www.nist.gov/pml/data/asd.cfm.
[26] Y. Torizuka, K. Hosaka, P. Schmidt, T. Odagiri, A. Knie, A. Ehresmann, R. Kougo, M. Kitajima, and N. Kouchi, Phys. Rev. A **99**, 063426 (2019).
[27] M. Glass-Maujean, The Journal of Chemical Physics **89**, 2839 (1988).
[28] K. Hosaka, K. Shiino, Y. Nakanishi, T. Odagiri, M. Kitajima, and N. Kouchi, Phys. Rev. A **93**, 063423 (2016).
[29] I. Borges and C. E. Bielschowsky, Journal of Physics B: Atomic, Molecular and Optical Physics **33**, 1713 (2000).
[30] M. Glass-Maujean and H. Schmoranzer, Journal of Physics B: Atomic, Molecular and Optical Physics **38**, 1093 (2005).
[31] M. Glass-Maujean, The Journal of Chemical Physics **85**, 4830 (1986), https://doi.org/10.1063/1.451717.
[32] M. Glass-Maujean, H. Frohlich, and P. Martin, Phys. Rev. A **52**, 4622 (1995).
[33] I. Borges and C. E. Bielschowsky, Chemical Physics Letters **342**, 411 (2001).
[34] M. Glass-Maujean, S. Klumpp, L. Werner, A. Ehresmann, and H. Schmoranzer, Journal of Physics B: Atomic, Molecular and Optical Physics **37**, 2677 (2004).
[35] J. D. Bozek, J. E. Furst, T. J. Gay, H. Gould, A. L. D. Kilcoyne, J. R. Machacek, F. Martín, K. W. McLaughlin, and J. L. Sanz-Vicario, Journal of Physics B: Atomic, Molecular and Optical Physics **39**, 4871 (2006).
[36] J. L. Sanz-Vicario, H. Bachau, and F. Martín, Phys. Rev. A **73**, 033410 (2006).
[37] K. Hosaka, Y. Torizuka, P. Schmidt, A. Knie, A. Ehresmann, T. Odagiri, M. Kitajima, and N. Kouchi, Phys. Rev. A **99**, 033423 (2019).
[38] S. L. Guberman, The Journal of Chemical Physics **78**, 1404 (1983), https://doi.org/10.1063/1.444882.
[39] D. Sprecher, C. Jungen, W. Ubachs, and F. Merkt, Faraday Discuss. **150**, 51 (2011).
[40] I. Sánchez and F. Martín, The Journal of Chemical Physics **110**, 6702 (1999), https://doi.org/10.1063/1.478576.
[41] J. Fernández and F. Martín, Journal of Physics B: Atomic, Molecular and Optical Physics **34**, 4141 (2001).
[42] M. Barat and W. Lichten, Phys. Rev. A **6**, 211 (1972).
[43] Y. V. Vanne, A. Saenz, A. Dalgarno, R. C. Forrey, P. Froelich, and S. Jonsell, Phys. Rev. A **73**, 062706 (2006).
[44] L. O. Santos, A. B. Rocha, R. F. Nascimento, N. V. de Castro Faria, and G. Jalbert, Journal of Physics B: Atomic, Molecular and Optical Physics **48**, 185104 (2015).
[45] G. Herzberg, *Spectra of diatomic molecules*, Molecular spectra and molecular structure (Van Nostrand, 1950).
[46] H. A. Bethe and E. E. Salpeter, *Quantum Mechanics of One- and Two-Electron Atoms* (Springer Berlin, Heidelberg, 1957).